Journal of Fluids and Structures 64 (2016) 87–106

Contents lists available at ScienceDirect

Journal of Fluids and Structures

journal homepage: www.elsevier.com/locate/jfs

Comparison of a RANS blade element model for tidal turbine arrays with laboratory scale measurements of wake velocity and rotor thrust

A. Olczak*, T. Stallard*, T. Feng, P.K. Stansby

School of Mechanical, Aerospace and Civil Engineering, University of Manchester, Sackville Street, Manchester, M13 9PL, UK

ARTICLE INFO

Article history:
Received 25 September 2015
Received in revised form
25 February 2016
Accepted 8 April 2016
Available online 19 May 2016

Keywords:
Tidal stream
Arrays
Wake
Experiment
CFD

ABSTRACT

A Reynolds averaged Navier Stokes (RANS) model has been compared with laboratory scale measurements of the loading and wake of arrays of horizontal axis three-bladed rotors. The diameter D of each rotor was 0.27 m and axis was at mid depth in a channel of depth $1.67D$ and width $11.5D$. Mean flow speed was 0.46 m/s, giving a Reynolds number of 2×10^5, with turbulence intensity of 12%. The commercial software StarCCM+ is employed. Steady flow is modelled and each rotor represented by imposing radial variation of streamwise force on the rotor defined by a blade element method. When experimental values of turbulent kinetic energy and dissipation rate are defined at the model inflow, the transverse profile of depth-averaged velocity of a single rotor wake is predicted reasonably for downstream distances greater than $4D$. Within $0.5D$ to $2D$ downstream of the rotor plane the wake is approximately axisymmetric and both streamwise velocity and wake rotation are reasonably well predicted for radii greater than half the rotor radius. Inclusion of tip generated turbulent kinetic energy as predicted by blade resolved RANS CFD improves predictions of streamwise velocity and wake rotation within $4D$ downstream. For a single row of rotors partially spanning the channel the increase of thrust coefficient relative to an isolated rotor due to global and local blockage is predicted, but the overall magnitude of thrust is overpredicted. Downstream of a single row the velocity deficit along the axis of each rotor is closely predicted while the deficit between adjacent wakes is underpredicted until approximately $8D$ downstream. For a second row of rotors located at $8D$ downstream the square of the rotor averaged velocity, indicative of thrust, is predicted to within 3% and 12% respectively for rotor axes aligned and staggered relative to those on the front row. For these downstream rotor positions similar accuracy may be obtained by superposition of the self-similar velocity deficit profile of isolated rotor wakes only. For multiple rows, thrust on the front row of rotors is increased relative to the same row in isolation. Rotors on downstream rows partly exposed to the higher velocity flow bypassing the array also experience high values of thrust. For arrays of up to twelve rotors the average thrust of an individual turbine in a row is typically predicted to within 10% for the first row and 20% for the second row and within 38% for the inner rotors of the third row. The accuracy of a RANS blade element method using commercially available software has thus been assessed for the complex wake flows of arrays of up to twelve three-bladed rotors in a shallow turbulent flow.

* Corresponding authors.
E-mail addresses: alex.olczak@windprospect.com (A. Olczak), tim.stallard@manchester.ac.uk (T. Stallard).

http://dx.doi.org/10.1016/j.jfluidstructs.2016.04.001
0889-9746/

1. Introduction

Tidal stream turbines are currently being developed for electricity supply. A variety of devices have been proposed but the most widely studied systems are horizontal axis turbines comprising a two or three-bladed rotor and typically supported on a rigid structure. System design requires accurate prediction of mean and unsteady loading on components. Unsteady blade loading occurs as the blade is rotated through a steady onset shear profile and due to time-variation of the onset flow caused by turbulence and waves. For large-scale electricity generation such turbines are expected to be deployed in long rows normal to the mean flow direction, i.e. fences, or in multiple rows, i.e. arrays. Prediction of loading of a turbine within an array thus requires adequate representation of the effect of ambient shear and turbulence on turbine loading and of the processes influencing development and interaction of turbine wakes within the array. Immediately downstream of a rotor the wake physics are complex, influenced by blade scale flow and tip vortex interaction with the supporting tower. Expansion of the wake profile and velocity recovery over longer distances downstream is due to mixing with the flow surrounding the wake. For a fence or array partially spanning a channel this differs between the flow around and through the array. A summary of the physical processes affecting the loading and wake of a turbine in isolation and within and array are given in Fig. 1. The extent to which these different processes may be represented with standard modelling approaches is briefly summarised in Table 1.

For a single turbine, mean and unsteady loading due to steady shear flows has been studied by various methods including blade element momentum theory (Way and Collier, 2013; Togneri et al., 2011) and RANS CFD (McNaughton et al., 2012; Fleming et al., 2013). Blade modelled Large Eddy Simulation (LES) studies with turbulent velocity fluctuations defined at inflow have provided some insight into the effect of turbulence on turbine loading (Afgan et al., 2013) and on noise generation (Lloyd et al., 2014). However, the high computational cost of such methods limits their application to single turbine loading, particularly if the domain resolution is to be sufficient for adequate resolution of ambient turbulence and wake recovery. Actuator line and disk methods have lower computational cost than blade modelled CFD so are attractive options for analysis of multiple turbines. Such approaches represent the force applied by the turbines as a momentum sink. Most simplistically, a constant force (F) can be applied to represent the net force of the rotor averaged over an actuator disk (Harrison et al., 2010). Or the radial variation of force ($F(r)$) may be defined using a Blade Element Momentum method (BEM), which when coupled to CFD is often known as RANS-BEM (see e.g. Edmunds et al., 2014). Alternatively the Actuator Line method applies the forces along lines representing the location of each turbine blade within an unsteady method (Sørensen and Shen, 2002; Schluntz and Willden, 2014). For these methods quasi-steady foil performance is assumed. In principle unsteady loads may be predicted due to flow variations over lengths much greater than the chord scale. Actuator line methods have been employed for simulation of load variation within arrays subject to onset turbulence (Churchfield et al., 2013) and blade loads on an individual turbine may be predicted to comparable accuracy to blade resolved CFD (Schluntz and Willden, 2014).

Semi-empirical wake models have been widely used for the representation of wind turbine wakes (Ainslie, 1988) and have been modified for tidal turbines (Parkinson et al., 2012). Comparison of the RANS-BEM method to experimental

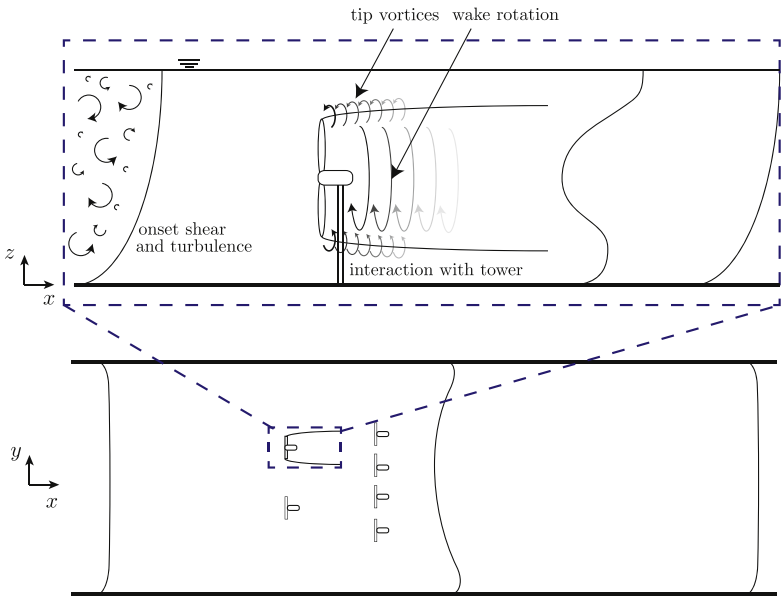

Fig. 1. Sketch of the flow processes affecting loading and wake of an isolated turbine and hence loading of turbines within an array.

Table 1
Summary of capabilities and typical applications of turbine wake modelling approaches.

Method	Predicted				Modelled					Applications
	Mean loads	Unsteady loads	Far-wake	Near wake	Wake rotation	Blade scale flow	Onset shear	Onset turbulence	Computational cost	
Linear momentum theory					Zonal idealisation				Low	Analytical
Blade element momentum theory (BEMT)	✓				No wake				Low	Fast numerical method for rotor design, inc. onset shear
RANS porous disc					N	N	Y	N	Med	Simple steady numerical model with far wake
RANS BEM	✓		✓		Y	N	Y	N	Med	Rotation, efficient, steady numerical model, up- stream shear
RANS actuator line	✓		✓	(a)	Y	N	Y	N	High	Unsteady, more efficient than blade resolved, up- stream shear
LES actuator line	✓	✓	✓	(a)	Y	N	Y	Y	v. high	Unsteady, wake length scales resolved
RANS blade resolved	✓	✓	✓	(a)	Y	Y	Y	N	v. high	Unsteady flow resolved
LES blade resolved	✓	✓	–	(a)	Y	Y	Y	Y	v. high	All flow scales resolved apart from sub grid

(a) - validation needed.

measurements of a turbine wake have generally shown reasonable agreement within the far-wake region (Bahaj et al., 2013; Masters et al., 2015) but improved understanding is required of the extent to which the near-wake may be predicted and of the limitations of RANS-BEM for simulating wakes in depth-constrained channel flows. Various RANS-BEM studies have been conducted of multiple tidal turbines (i.e. Malki et al., 2014; Turnock et al., 2011 and Edmunds et al., 2014). However to-date there have been few studies of the accuracy of both load and wake prediction relative to experimental data. Through comparison to experimental measurements of the wakes of up to three turbines, Masters et al. (2013) found that a RANS-BEM simulation with $k-\omega$ turbulence closure model is capable of predicting flow velocity structures within the mid to far wake regions to an acceptable level of accuracy. Similar agreement has also been demonstrated with experimental measurements of the wake of three side-by-side rotors and two in-line rotors using RANS-BEM simulation with $k-\omega$ SST turbulence closure model (Shives and Crawford, 2014).

The recovery of the far wake is known to be dependent on ambient turbulence (e.g. Ainslie, 1988). However, recovery of velocity from immediately downstream of the rotor also depends on the radial variation of momentum extraction, the rotation of the wake and the structure of tip vortices. Tip vortices correspond to a region of enhanced turbulent kinetic energy (TKE) near the blade tip, the magnitude of which has been measured at laboratory scale (Tedds et al., 2012) and obtained from blade modelled simulations (Afgan et al., 2013). To-date most actuator CFD studies have applied TKE at the inlet boundary only in order to reproduce the levels of turbulence intensity measured experimentally (Bahaj et al., 2013; Harrison et al., 2010). A turbulence source may also be defined at the turbine to represent the enhanced turbulence associated with operation. Such sources have been defined as constant over the disc area based on an empirical relation (Bahaj et al., 2013) or at the disc circumference to represent tip vortices (Nishino and Wilden, 2012). It has been shown that blade induced turbulence increases the loading and power output of turbines within a fence partially spanning a channel (Nishino and Willden, 2012) due to increase of effective blockage.

This study addresses the accuracy with which a RANS-BEM model predicts the downstream velocity field and streamwise loading of both an individual turbine and of small groups of up to twelve turbines. Evaluation is by comparison to experimental measurements of the velocity field and individual turbine loading obtained using three-blade tidal stream rotors in a shallow, turbulent flow. The experimental approach and array configurations studied are introduced in Section 2. The RANS-BEM model is described in Section 3. Comparison to measurements for a single turbine are given in Section 4 both in terms of loading and wake velocity field. The flow-field downstream of a single row of rotors is compared to experimental measurements in Section 5; the agreement with measured velocity profile and the rotor averaged velocity incident to downstream turbine locations is quantified. Comparison is also made to the wake profile obtained by superposition of a self-similar velocity deficit profile that represents the transverse profile of the far wake of a single turbine. Prediction of individual turbine loading and downstream wake prediction is assessed for a number of two and three row arrays in Section 6.

2. Experimental study

The experimental arrangement is as described for studies of the flow downstream of a single rotor and a single row of rotors in a shallow, turbulent flow (Stallard et al., 2015, 2013). Details of the instrumentation and a wider array-wake study have previously been reported (Thomson et al., 2011). The general arrangement is briefly described here with reference to Fig. 2. Experiments were conducted with turbines of diameter D=0.27 m in a channel of width $W = 18.5D$ and with depth $d = 1.67D$. A left-handed global co-ordinate system is used in which X is aligned with the direction of the flow, Y is horizontal across the width of the flume and Z is vertical (positive upwards). The origin $(X, Y, Z) = (0, 0, 0)$ was defined as $22D$ from the flume inflow, at mid-span and mid-depth, coincident with the axis of the central rotor on the front row. For a single rotor, global blockage as defined by ratio of swept area to channel cross section (A_D/Wd where $A_D = \pi D^2/4$) is 2.5% and wake expansion is effectively unconstrained in the transverse direction but is constrained vertically by the bed and free surface. The widest single row layout comprises five rotors at transverse centre to centre spacing $Y_{sp} = 1.5D$. For this layout the local blockage is 31% ($A_D/Y_{sp}d$) and global blockage 12.5% ($5A_D/Wd$) and so a measurable increase of thrust coefficients and of bypass flow velocity are expected.

Time varying velocity components (u_x, u_y, u_z) are measured using NORTEK Acoustic Doppler Velocimeter (ADV) Vectrino+ with 200 Hz sample rate. Mean velocity components (U_x, U_y, U_z) and turbulence intensities are subsequently obtained. The probes are orientated with their local x-axis aligned with the global X-axis. The experiments were designed for a mean velocity of approximately 0.45 m/s. The Reynolds number based on turbine diameter is thus greater than 1.2×10^5 and so wake velocity and turbulent statistics are expected to be Reynolds number independent (Chamorro et al., 2012). Measurement of the mean flow and turbulence characteristics taken at the plane of a single rotor or first row (X=0) indicate that the vertical profile of mean velocity follows the log-law Eq. (1), where $z' = z + d/2$ is the distance from the bed) with friction velocity $U_* = 0.0187$ m/s, von Karman constant $\kappa = 0.41$ and C=5:

$$\frac{U(z')}{U_*} = \frac{1}{\kappa}\log\frac{z'U_*}{\nu} + C \tag{1}$$

Depth average turbulence is 12% in the streamwise direction and 9% in the vertical and lateral directions. The integral length scales of the ambient turbulence measured by a two point cross correlation method (Pope, 2000) at mid-depth are 0.56 h, 0.33 h and 0.25 h in the streamwise, transverse and vertical axes respectively. Sample duration was 900 s for these measurements. Length-scales were also estimated by an auto-correlation method providing similar values at mid-depth. It is well known that horizontal scales are greater than vertical in shallow flows and these scales are of similar magnitude to field measurements. However, such parameters vary widely (Thomson et al., 2012; Sutherland et al., 2013) and so may only be considered representative of conditions that may be experienced by a tidal stream turbine during operation.

Streamwise thrust, applied torque and rotational speed of each rotor were sampled at 200 Hz. Each rotor was supported on a 90° bevel gearbox coupled to a dynamometer located above the waterline. Angular speed (Ω) is defined as the rate of change of angular position which was measured using a HEDS 9000 quadrature encoder reading an HEDM 6120 T12 code wheel. The dynamometer applied a retarding torque such that each rotor operated with an average tip speed ratio ($\lambda = \Omega R/U_0$) of 4.5 due to the ambient flow. A three-bladed rotor was employed with each blade defined by a Göettingen 804 section. This aerofoil section was selected as it develops high lift to drag ratio at the moderate chord Reynolds number of these experiments ($Re_c = 0.75\Omega Rc/\nu \sim 30,000$ at three-quarter radius). Radial variation of pitch angle and chord length, c,

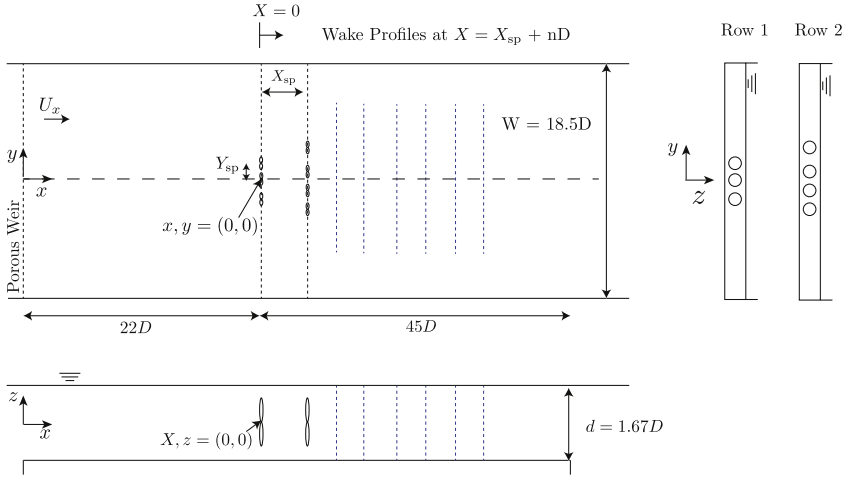

Fig. 2. General arrangement of experiment for array layout 2row34-X_{sp}4D as described by Table 2. Not to scale.

were selected to represent the variation of thrust coefficient with tip-speed-ratio of a full-scale rotor (Whelan and Stallard, 2011; Stallard et al., 2015). The supporting tower extended to mid-depth, was circular with 15 mm external diameter and axis located 50 mm downstream of the rotor plane. Streamwise thrust on the rotor was determined from the total force measured via a full-bridge strain gauge located at the top of the support structure and reduced by the drag measured on the supporting tower (Stallard et al., 2015). Drag on the tower due to the onset flow only was measured to be less than 10% of rotor thrust and so this minimal structure is not expected to significantly influence the rotor wake. This is supported by measurements of a single rotor wake in which the tower wake is evident at 0.5 D downstream but is indistinguishable from the rotor wake by one diameter downstream.

2.1. Single rotor

Experimental measurements of a single rotor wake (Stallard et al., 2015) show that wake generation and recovery in a shallow flow can be considered in several regions, as sketched in Fig. 3. The onset flow to the turbine is sheared and turbulent (a). At the rotor plane (b) a wake is generated by extraction of momentum from the flow. The near wake region is characterised by wake rotation and can be considered as an approximately axisymmetric shear layer (c). This shear layer expands with distance downstream with a rate which is greater in the transverse direction than the vertical direction, although this will be dependent on depth to diameter ratio. Following a transition region (d) the velocity profile can be characterised as an expanding two dimensional Gaussian profile (e) in the transverse direction. For this experimental arrangement region (c) was observed to extend to around two diameters downstream. Over the far-wake region (e), the transverse profile of depth-averaged velocity deficit is self-similar and follows Eq. (2). For these experiments the recovery of velocity deficit, ΔU_{max}, and expansion of half width, $y_{1/2}$, followed Eq. (3) for downstream distances $X > 8D$:

$$\frac{\Delta U_x(y)}{\Delta U_{max}} = \exp\left(-\ln 2\frac{y^2}{y_{1/2}^2}\right) \tag{2}$$

$$\frac{\Delta U_{max}}{U_0} = 0.864\left(\frac{x}{D}\right)^{-\frac{1}{2}} - 0.126 \quad \text{and} \quad \frac{y_{1/2}}{R} = 0.412\left(\frac{x}{D}\right)^{\frac{1}{2}} + 0.5 \tag{3}$$

2.2. Single and multiple rows of rotors

Experimental measurements of rotor angular speed, rotor thrust and wake velocity were obtained for eleven different layouts with between two and twelve turbines. The array layouts are listed in Table 2 and an example of a layout shown in Fig. 2. For each rotor constant retarding torque was applied by a dynamometer system and defined to develop a tip-speed-ratio of 4.5 when in isolation. For each array layout lateral profiles of velocity at mid-depth were obtained from samples of 60 s duration recorded at between 41 and 81 y-ordinates over a range exceeding the width of the downstream row of the array. As a minimum profiles were measured at locations two- and four-diameters downstream of the final row of each array. Vertical profiles were also obtained from samples of 60 s duration obtained at 20 to 40 z-ordinates at the same downstream locations and aligned with the y-ordinate of the rotors on the final row of the array. The total number, N, of 60 s samples available for each array layout is listed in Table 2.

Each of the set of 20–81 samples recorded during a particular wake traverse was processed to obtain the mean velocity, turbulence intensity and Reynolds stresses at the corresponding velocity measurement co-ordinate. The set of all N samples recorded during all traverses conducted for a particular array layout was processed to obtain the mean and standard deviation of the thrust and angular speed of each rotor. During each wake traverse, streamwise force, torque and rotational speed for each rotor were also synchronised with the velocity measurement at each sample point. Thrust applied to each rotor was obtained as the measured force offset by a nominal tower load as for a single turbine, neglecting variation of tower drag with wake profile and rotor location. Herein wake velocities, rotor thrust and tip-speed ratio are reported relative to the onset flow velocity U_0.

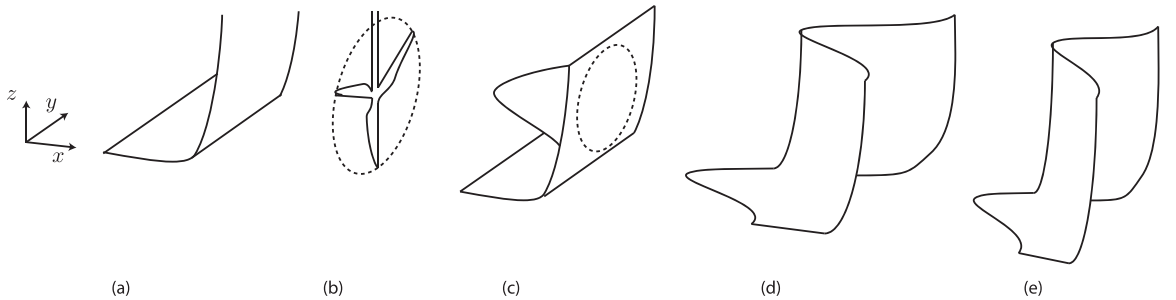

Fig. 3. Sketch of development of streamwise velocity profile from (a) upstream shear profile, incident to (b) rotor leading to development of (c) initially axisymmetric wake a short distance downstream of rotor plane and (d and e) transverse Gaussian profile and recovery to shear profile far downstream.

Table 2
Summary of turbine configuration and velocity measurement locations for the eleven different array layouts studied. Name of each layout defined as: **n row m1 m2 - Y_{sp}xD or - X_{sp}xD** where n is number of rows, m1 is number of turbines in row 1, m2 number of turbines in row 2, Y_{sp} the lateral spacing between adjacent rotor axes on each row and X_{sp} the streamwise spacing between each row. Spacing in each axis is expressed as multiple of the rotor diameter, xD. Staggered indicates that axis of rotors on downstream row offset by $Y_{sp}/2$ from the axis of rotors on preceding row (e.g. Fig. 2). Aligned indicates that the rotors on downstream rows are inline with the axis of rotors on the preceding row (e.g. Fig. 4).

Name		Y_{sp}	X_{sp}	N	Location, X, of wake profiles					
					2D	4D	6D	8D	10D	12D
1row2-Y_{sp}1.5D	–	1.5	–	136	✓	✓				
1row2-Y_{sp}2D	–	2	–	136	✓	✓				
1row2-Y_{sp}3D	–	3	–	134	✓	✓				
1row3-Y_{sp}1.5D	–	1.5	–	419	✓	✓	✓	✓	✓	✓
1row3-Y_{sp}2D	–	2	–	191	✓	✓				
1row3-Y_{sp}3D	–	3	–	163	✓	✓				
1row5-Y_{sp}1.5D	–	1.5	–	470	✓	✓	✓	✓	✓	
2row55-X_{sp}8D	Aligned	1.5	8	254					✓	✓
2row34-X_{sp}4D	Staggered	1.5	4	173			✓	✓		
2row34-X_{sp}8D	Staggered	1.5	8	183					✓	✓
3row345-X_{sp}4D	Staggered	1.5	4	172					✓	✓

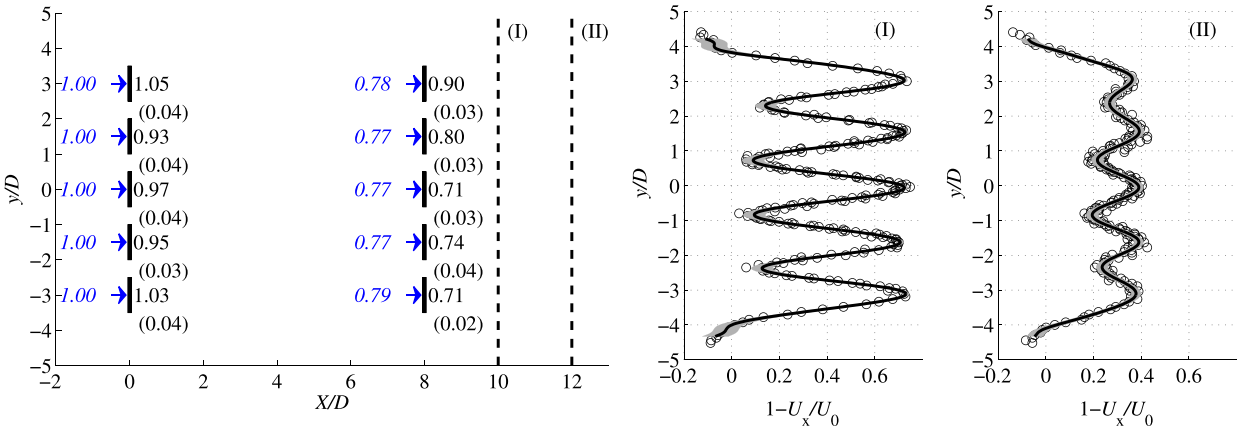

Fig. 4. Arrangement of two rows of five rotors (array layout 2row55-X_{sp}8D) showing mean thrust co-efficient, $\overline{C_T(N)}$, (black text) and standard deviation of mean values, $\sigma(\overline{C_T}(N))$ (black text in brackets), for each rotor in array. Blue arrow indicates normalised disk averaged velocity (U_D/U_0, blue text) at the location of each rotor. Wake measurements at $X = 10D$ (I) and $12D$ (II) obtained from one minute average velocity deficit, $1 - U_x/U_0$ (○) with polynomial best-fit (▬) and ± one standard deviation of mean values (shaded).

An example of the measured wake profiles and corresponding thrust coefficients for an array comprising two rows of five rotors at longitudinal spacing $X_{sp} = 8D$ (denoted 2row55-X_{sp}8D) is shown in Fig. 4. Wake profiles are shown as the time-average for each location within the wake (obtained from each 60 s second sample) and with a polynomial best fit (the order of which was selected to obtain least-squares-best-fit to the measured mean velocity). The uncertainty range associated with the standard deviation of measurements relative to the best-fit is also shown. Numerical predictions of array wakes are evaluated against the best-fit wake profiles.

Since the square of the disc averaged velocity defines rotor thrust ($F \propto U_D^2$) this velocity is employed as a metric for quantifying the accuracy of downstream velocity prediction by RANS-BEM modelling. The onset velocity onto each rotor (U_D/U_0) is shown in Fig. 4. For the front row of rotors the undisturbed flow represents the onset velocity ($U_D/U_0 = 1$). For the second row of rotors the onset flow was determined from the wake measurements taken downstream of the first row that are within the swept area of downstream rotors. i.e. for the 2row55-X_{sp}8D case the disk averaged velocity was obtained from the velocity measurements obtained 8D downstream of the 1row5-Y_{sp}1.5D array layout.

Disk average velocities U_D were obtained at the location of rotors on the second row with axis at (X_D, Y_D, Z_D) by Eq. (4). For rotor locations aligned with the axis of rotors on the upstream row, velocity samples within the swept area comprise a set of n_y velocity measurements at positions y_i and spacing dy from the lateral profile and n_z velocity measurements at locations z_j at spacing dz from the vertical profile. For these aligned rotor locations each sample was assumed to represent the velocity over a quarter of the area of the annulus in which it was measured, e.g. $A_i = \pi/4[(y_i + dy/2)^2 - (y_i - dy/2)^2]$ and similarly for A_j as a function of z_j. For rotor locations staggered relative to the axis of rotors on the upstream row, a vertical profile was not measured. For these locations $n_z = 0$ and disc averaged velocity was obtained from the weighted average of the set of n_y velocity

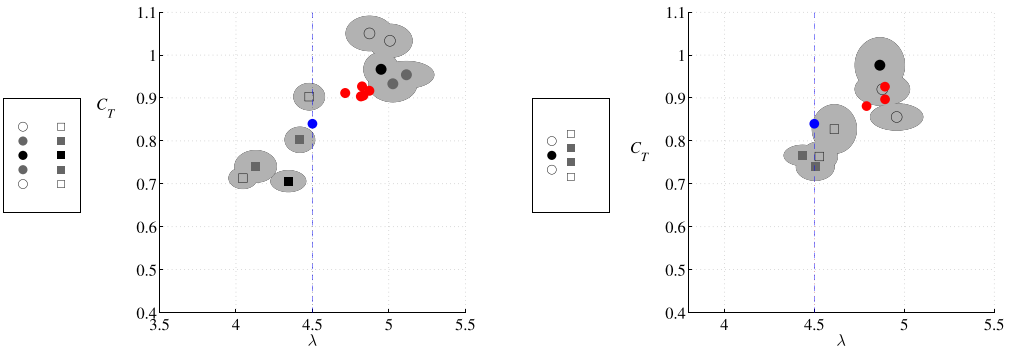

(a) Layout **2row55-X$_{sp}$8D** with comparison to single row layout 1row5-Y$_{sp}$1.5D

(b) Layout **2row34-X$_{sp}$4D** with comparison to single row layout 1row3-Y$_{sp}$1.5D

Fig. 5. Mean thrust co-efficient ($\overline{C_T(N)}$) and tip-speed ratio $\overline{\lambda(N)}$ for each rotor within array of two rows of rotors. Mean values also shown for the single row layout that comprises the front row of each array (●) and for isolated rotor with tip speed ratio of 4.5(●). Shaded regions denote range of all time-average samples for each rotor for this configuration.

measurements only assuming each sample represents the velocity over a vertical strip of width dy centered at y_i with area $A_i \sim 2(R^2 - (y_i - Y_D)^2)^{1/2}dy$. For integration over more than 30 velocity measurements within the swept area, this approach provides disc averaged velocity to within 1% and 2% for aligned and staggered rotor locations beyond $4D$ downstream:

$$U_D = \frac{1}{A_D}\sum_{i=1}^{n_y} U_x(y_i)A_i + \frac{1}{A_D}\sum_{j=1}^{n_z} U_x(z_j)A_j \tag{4}$$

The thrust coefficient of each rotor is presented as the mean ($\overline{C_T(N)}$) and standard deviation ($\sigma(\overline{C_T}(N))$) calculated from all N one minute samples listed for each array layout in Table 2. Fig. 5 shows the same thrust coefficient variation in addition to the mean and standard deviation of the tip-speed ratio defined as $\overline{\lambda(N)}$ and $\sigma(\overline{\lambda}(N))$ respectively. Variation of mean thrust with location in the array is evident from Figs. 4 and 5. Rotors on the front row develop a higher thrust coefficient than an isolated rotor. This is partly due to the greater values of global and local blockage, resulting in an onset flow velocity that is higher for these rotors than for an isolated rotor and to an increased velocity bypass flow. The angular speed of the rotors on the front row is also increased due to the application of the same constant retarding torque. A slightly greater increase in angular speed is observed for rotors on the first row of a two row array than the equivalent single row array (Fig. 5) consistent with higher velocity across the front row due to the higher net thrust of the array as a whole. Rotors on downstream rows develop lower C_T than those on the front row. This reduction in force is caused by both a reduction of onset velocity, to approximately $0.78U_0$ for the second row of rotors, and a reduction of rotational speed due to the application of constant torque.

Assuming that the velocity local to a rotor defines its wake, then superposition of the deficit profile defined by Eq. (2) for each rotor provides a simple approach for estimating the transverse profile of streamwise velocity downstream of a single row. This approach does not directly account for blockage but this may be incorporated using classical aerodynamic methods such as Maskell (1965) or by imposing mass flux conservation. Comparison of this superposition approach with an array bypass velocity defined for mass flux conservation is shown in Section 5 and further evaluation of this approach for multi-row arrays is given by Stansby and Stallard (2016).

3. RANS-BEM model

A RANS-BEM method has been implemented in the CFD code StarCCM+. The k$-\omega$ SST turbulence model was used which has been observed to provide accurate prediction of actuator disc wakes relative to several alternative models (Shives and Crawford, 2014). The blade element model is written as a user C code and the source terms are updated within every solver iteration. The source terms are calculated by application of the BEM over multiple concentric annuli each of width dr with centre at radius r and which form a disk of area equal to that of the swept area of a rotor (Fig. 6a). The source terms comprise a radial variation of axial and tangential force, each a function of both the angle of incidence (ϕ) and magnitude of the velocity (V) relative to the rotor plane at the centre radii of each annulus. The angle of incidence $\phi = \alpha - \beta$, where α is the angle of attack and β is the twist of the chord, of length c, relative to the rotor plane. The velocity magnitude is given by $V = [(U_0(1-a))^2 + (\Omega r(1+a'))^2]^{1/2}$ (Fig. 6b). The radial variation of force $F(r, \phi, V)$ in the streamwise (x) and azimuthal (θ) directions is given by Eqs. (5) and (6) where $\sigma = 3c/2\pi r$ describes the solidity of each annulus. Both twist angle and chord length vary with radius as tabulated in Stallard et al. (2015). Variation of lift coefficient C_l and drag coefficient C_d with angle of attack (α) are from the same source based on the experimental data of Miley (1982). Thus:

$$dT = \rho\sigma\pi V^2(C_l \cos\phi + C_D \sin\phi)r\, dr \tag{5}$$

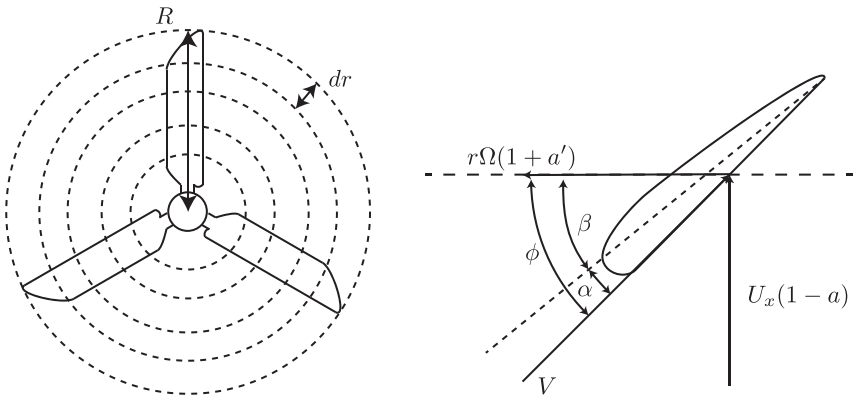

(a) Rotor divided into concentric annuli

(b) Blade diagram showing angle (ϕ) and magnitude (V) velocity onto each blade segement

Fig. 6. Blade element momentum method.

$$dQ = \rho\sigma\pi V^2 r^2 (C_l \sin\phi - C_D \cos\phi)\, dr \tag{6}$$

Radial coefficients of streamwise thrust and torque are defined as $dC_T = dT/0.5\rho A U_0^2$ and $dC_Q = dQ/0.5\rho A U_0^3$. Rotor averaged thrust and power coefficients are given by $C_T = \int_0^R dC_T\, dr$ and $C_P = \Omega \int_0^R dC_Q\, dr$. A Prandtl tip-loss correction factor (Hansen, 2008) is applied since the annular model does not represent discrete blades. The momentum source terms are applied to the disk area which is discretised as a structured polar mesh. The hub is modelled as a solid cylinder with radius as in the experiment and with hemispherical front. The supporting tower used in the experiments is not modelled since the deficit has been shown to be small relative to the rotor wake at a typical operating point. Inlet velocity is prescribed as the depth average of the measured velocity profile (Eq. (1)), $U_0 = \overline{U_x(z)}$. To minimise the computational cost a relatively coarse mesh is used for the outer domain and the mesh is refined around the disk and within the wake over the region $-3D < X < 15D$ and $-2D < Y < 2D$. In this region 17 annuli were employed over the swept area with a cell size of $dx = d/18$ and $dy = dz = d/36$. All simulations were run until StarCCM+ convergence criteria on continuity and the x, y and z momentum were all less than 1×10^{-3}. Convergence was confirmed by conducting simulations with a finer mesh ($dx = d/36$ and $dy = dz = d/72$).

3.1. Rotor loading and wake generation

The generation of a wake is governed by momentum extraction, and is therefore dependent on thrust co-efficient (C_T). Initial simulations were conducted to assess the accuracy of mean thrust prediction. Simulations were performed in low blockage domains ($A_D/Wd = 0.8\%$) with low turbulence to allow comparison with a blade element momentum theory (BEMT) code. The predicted thrust and power co-efficient (C_P and C_T) for a range of tip-speed ratios (λ) are presented for the flume experiments (Section 2) and a published tow-tank test (Bahaj et al., 2007) (Fig. 7). Thrust and power coefficient are generally higher than BEMT prediction for both of the rotors considered although similar for the flume experiments at tip-speed ratio of 4.5, for which wake comparisons are presented in Section 4. For the flume geometry and low turbulence there is a small increase of both C_T and C_P for $\lambda > 4$. Similar discrepancy has previously been reported for RANS-BEM (Bahaj et al., 2013) relative to towing tank experiments. Both coefficients are slightly higher again with onset turbulence representative of the experiments and wake expansion constrained by the depth; power coefficient is overpredicted by a factor of two whilst thrust coefficient is within 8% for the tip-speed ratio of $\lambda = 4.5$.

The radial variation of streamwise force and in-plane torque coefficients imposed by the RANS-BEM for $\lambda = 4.5$ are presented in Fig. 8. Variation is consistent with BEMT predictions for axial force although there is a higher prediction of the tangential force resulting in a higher value of C_P at this tip-speed ratio (Fig. 7a). The initialisation of the wake at the rotor plane can be determined by the radial variation of induction factor ($a = 1 - U_D/U_0$) which defines the velocity at the disc U_D relative to the free stream velocity (U_0). For $r/R < 0.8$ the axial induction factor agrees with that obtained from BEMT. The discrepancy at the tip is caused by the different numerical application of a tip correction. The RANS-BEM reduces the applied force and thus increases flow through this region. Tangential induction factor ($a' = U_\theta/\Omega r$ where U_θ is the tangential component of velocity and Ω is the rotor angular speed) at the rotor plane is greater for RANS-BEM than BEMT (Fig. 9b); this is due to the greater magnitude of applied torque.

3.2. Ambient and blade generated turbulence

Two applications of turbulence are considered: application of turbulence at the upstream (inlet) boundary and application of turbulence at the rotor plane. For the inlet turbulence case depth-averaged values of turbulence intensity $TI = 12\%$ and length scale $L = d/2$ were applied by specification of turbulent kinetic energy TKE ($k = \frac{3}{2}TI^2U^2$) and specific turbulence

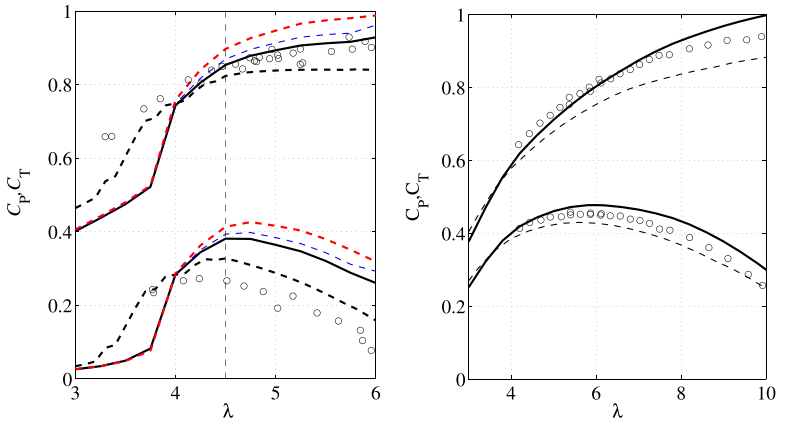

(a) 0.27 m diameter rotor Stallard et al., 2015 (b) 0.8 m diameter rotor Bahaj et al., 2007

Fig. 7. Mean thrust (C_T) and power (C_P) coefficients for a range of tip-speed ratios. Experiments (o), RANS-BEM with low blockage (0.8%) and low-turbulence (▬), RANS-BEM with channel geometry (blockage 2.5%) and low turbulence (- - ·), RANS-BEM with channel geometry and high turbulence (TI=0.12 and $L = d/2$) (- - ·) and BEMT (- - ·).

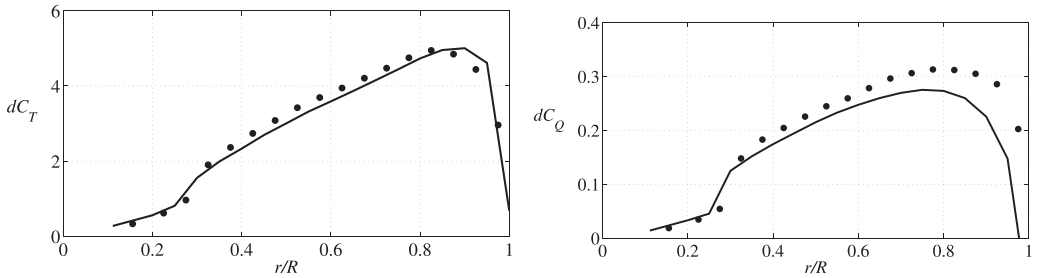

Fig. 8. Applied radial variation of force and torque for $\lambda = 4.5$. RANS-BEM (●) and BEMT (—).

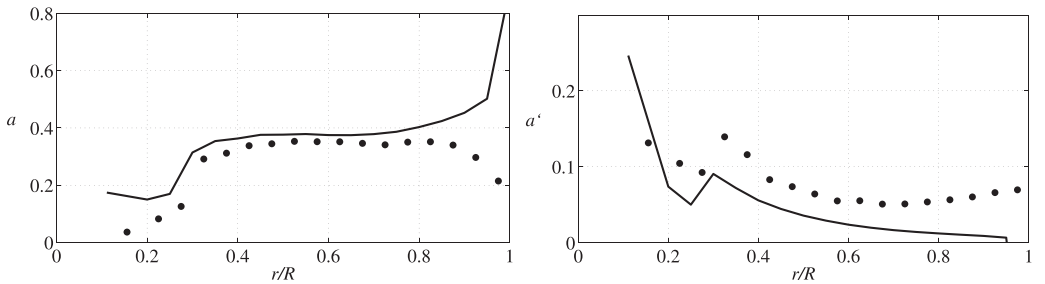

Fig. 9. Axial induction factor (a) at rotor plane ($X = 0D$) for $\lambda = 4.5$. RANS-BEM (●) and BEMT (—).

dissipation rate ($\omega = k^{\frac{1}{2}}[C_\mu L]^{-1}$, where C_μ is a constant equal to 0.09). Tip-generated turbulence can be included through application of a source of TKE at the rotor plane. To investigate the relative influence of ambient turbulence and blade generated turbulence on wake recovery, comparison is made with the wake from a blade modelled RANS $k-\omega$ SST CFD study (Afgan et al., 2013). Ambient turbulence is defined by $TI = 1\%$ and $L = 0.7D$. Tip-generated turbulence is applied in the RANS-BEM model as a Gaussian function $S_K = \exp((r-R)^2(2W)^{-2})$ (Fig. 10(a)) where S_K and W are the magnitude and width of the source and are selected such that the TKE at $X = 0.4D$ is equal to that given in Afgan et al. (2013). The TKE applied at the rotor plane dissipates downstream and therefore the magnitude and distribution of the source required to give the appropriate value at a location downstream $X = 0.4D$ is dependant on the dissipation rate.

The influence of ambient and tip-turbulence on wake recovery is shown in Fig. 10. Discrepancies between both RANS-BEM simulations and the blade resolved simulation near the centreline of the wake are due to inclusion of a tower in the blade resolved model. For downstream locations $X < D$ tip-turbulence has little effect on the wake, however this greatly

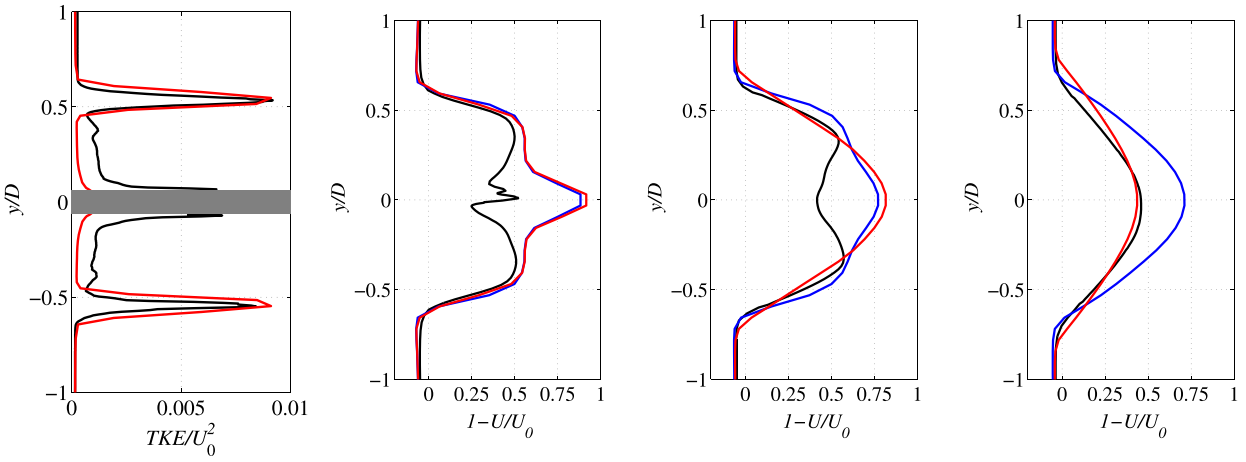

Fig. 10. Vertical profile of (a) turbulent kinetic energy representing blade resolved model and (b–d) velocity deficit further downstream by RANS-BEM (no sources)(——), RANS-BEM (TKE source)(——) and Blade modelled (Afgan et al., 2013) (——).

improves the agreement of wake width at $X = 4D$ and $X = 9D$. At $X = 9D$ the model with added turbulent sources provides much better agreement with the blade-resolved simulation.

4. Prediction of single rotor wake

Predictions of the velocity and turbulence downstream of a single rotor are compared with the experimental measurements summarised in Section 2.1 for inflow turbulence, defined to represent the experimental flow, or tip generated turbulence as outlined in Section 3.2 or for combined inflow turbulence and tip-generated turbulence. Accuracy of the RANS-BEM methods is presented for the near and far wake regions and the effect of water depth on the transition to the far wake is studied.

4.1. Far wake

Ambient turbulence at the inlet produces vertical and transverse wake profiles in agreement with experimental measurements for downstream distances $X > 4D$ (Fig. 11(b–d) and Fig. 12(b–d)). Tip-turbulence applied with the same ambient turbulence results in rapid dissipation of TKE from the elevated level at $X = 0.4D$, becoming similar to the ambient level by $X = 8D$ (Fig. 12(g)). This causes the far wake velocity to be similar to the case with inlet turbulence only. Tip turbulence

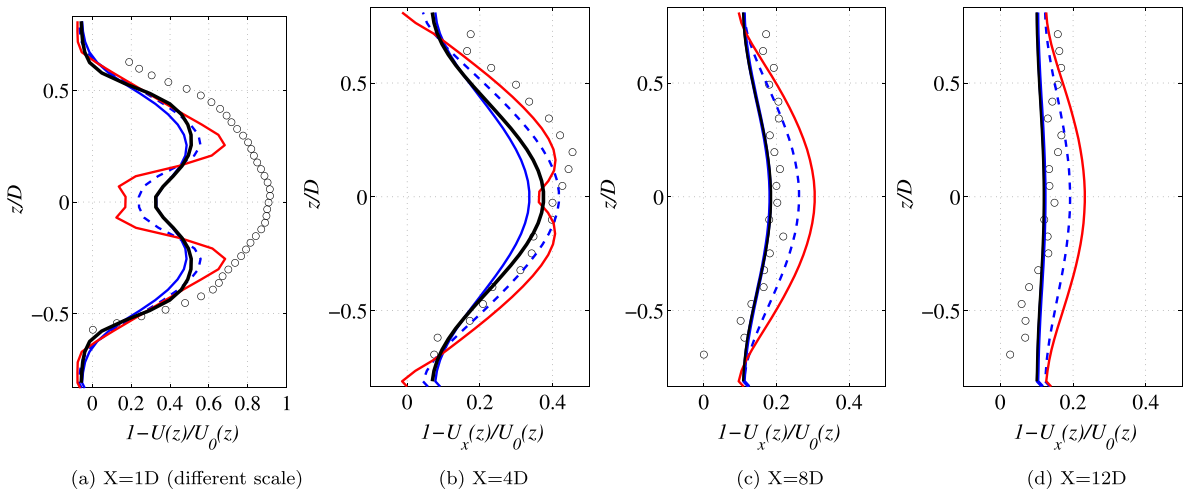

Fig. 11. Vertical profiles of streamwise velocity $U_x(z)$ by RANS-BEM with Inlet-Turbulence (——), Tip-Turbulence (——), Tip+Inlet Turbulence ($L = d/2$) (——), Tip+Inlet Turbulence ($L \approx$ chord)(- - -) and from experiment (o). Onset velocity $U_0(z)$ is constant with depth for RANS-BEM predictions and defined by Eq. (1) for experimental data.

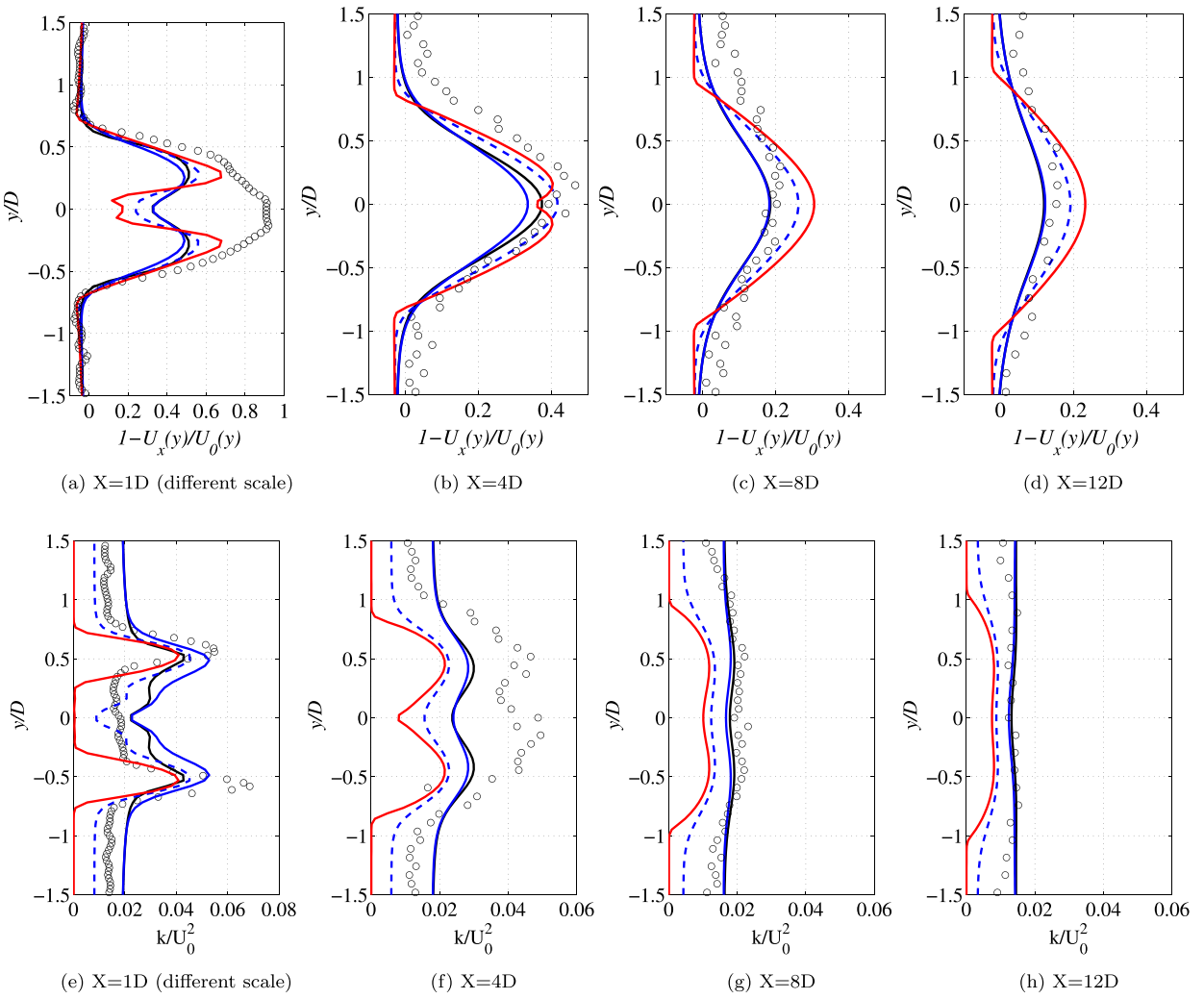

Fig. 12. Lateral profiles of streamwise velocity (a–d) and Turbulent Kinetic Energy (e–h) for the same cases as Fig. 11.

applied with inlet turbulence defined by $TI = 1\%$ and $L = 0.7D$ dissipates over a longer distance, however the magnitude of kinetic energy within the wake is lower than measured experimentally which results in less recovery by $8D$ downstream and beyond. Table 3 summarises the accuracy to which each of the methods predicts the lateral wake profiles. Inclusion of tip turbulence leads to a slight reduction in discrepancy at $4D$ but an increase at $8D$.

The far-wake model of Eqs. (2) and (3) describes the lateral profile of velocity at mid-depth downstream of a single rotor for locations $X > 8D$. Over this range, the velocity at mid-depth was found to closely approximate the depth-averaged velocity. For the same depth to diameter ratio ($d = 1.65D$) the RANS-BEM prediction of velocity at mid-depth is within 5% of the depth averaged velocity beyond $8D$ downstream and within 1% beyond $13D$ downstream indicating a somewhat longer wake recovery distance (Fig. 13). For the same rotor operating point, the distance over which the centreline velocity recovers to the depth-averaged velocity is reduced for smaller values of depth, with similar recovery distance to the experimental measurements for depth of 1.1D.

4.2. Near wake

The application of an axial and tangential force causes both a deficit of axial velocity and induces tangential velocity. Wake profiles over the far-wake region are predicted to similar accuracy by either turbulence approach, depending on the dissipation rate applied although tip-turbulence results in a lower wake velocity than ambient turbulence only. For $X < 4D$ (Figs. 11 and 12) tip-turbulence improves agreement with experimental measurements of wake velocity and width. For $X = 0.5D$ the model with tip-turbulence predicts lower velocity, similar to the experiments, at around half radius (Fig. 14). For larger radii the velocity variation is similar but the wake is narrower without tip-turbulence. Neither method accounts for the low velocity region close to the centre of the wake that is largely due to the supporting circular tower and sharp-

Table 3
Percentage discrepancy between RANS-BEM prediction and measured profile of velocity downstream of single rotor.

Approach	Turbulence			Discrepancy	
	At inlet		At tip	*4D*	*8D*
	TI(%)	L			
Inlet turbulence only with half depth length scale	12	d/2	No	7.7	3.5
Inlet turbulence with half depth length scale and tip turbulence	12	d/2	Yes	8.3	3.5
No inlet turbulence with tip turbulence	1	0.01	Yes	6.6	6.7
Inlet turbulence with chord length scale and tip turbulence	12	0.02	Yes	6.4	4.9

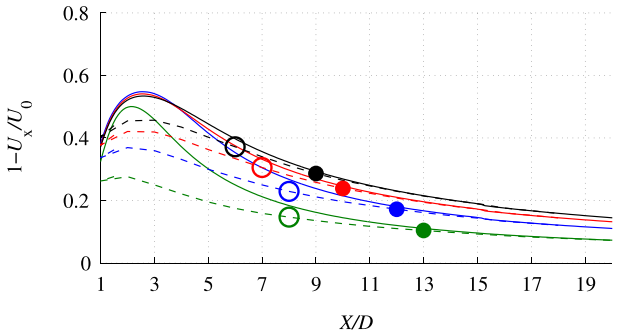

Fig. 13. Comparison of deficit of both mid-depth velocity, $1 - U_x(z = d/2)/U_0$ (—) and depth averaged velocity $1 - \overline{U_x(z)}/U_0$ (– – ·) from RANS-BEM for depth $d = 1.65D$(—), $1.4D$(—), $1.2D$ (—) and $1.1D$ (—). Integer distance at which mid-depth velocity within 5% (○) and 1% (●) of depth averaged velocity indicated.

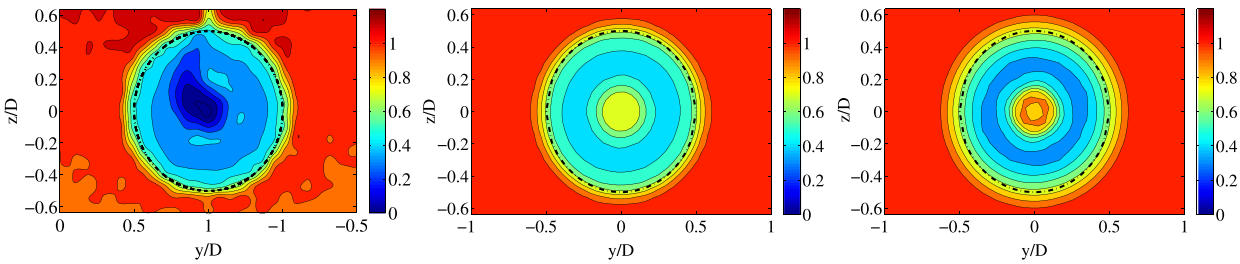

(a) Experiments (b) RANS-BEM - Inlet Turb. (c) RANS-BEM - Tip Turb.

Fig. 14. Mean of streamwise velocity (U_x) over vertical YZ plane of the near wake at $X = 0.5D$.

edged nacelle, neither of which are modelled.

Tangential velocity is similar for both methods at $X = 0.5D$ except that the inclusion of tip-turbulence captures a band of higher tangential velocity at around half radius (Fig. 15). This is similar to the experimental measurement at the same downstream plane and underpredicted with ambient turbulence only. At this radius rotation persists further downstream than without tip-turbulence (Fig. 16). However, at larger radii tangential velocity is similar by both methods beyond $X = 1D$ downstream.

5. Single row of turbines

The loading and wake of a single row of rotors partially spanning the width of the channel is modelled using the RANS-BEM method of Section 3. Accuracy is assessed on the basis of the predicted thrust coefficient for each rotor in the array and the square of velocity over the fluid area corresponding to the location of downstream rotors of multi-row configurations. This rotor averaged velocity is an indicator of the thrust experienced by each downstream rotor $F \propto U_D^2$ and was obtained by the two methods described in Section 2.2. These disc averaged velocities represent the inflow to the rotors on downstream

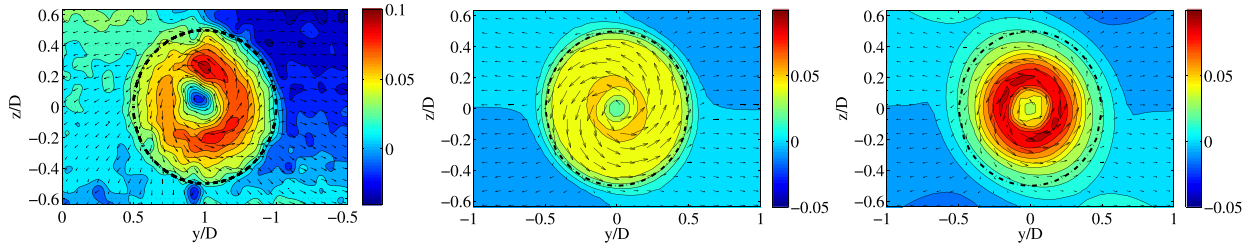

(a) Experiment (b) RANS-BEM - Inlet Turb. (c) RANS-BEM -Tip Turb.

Fig. 15. Tangential velocity (U_θ) over vertical YZ plane of the near wake at $X = 0.5D$. Velocity components U_z, U_y shown as arrows.

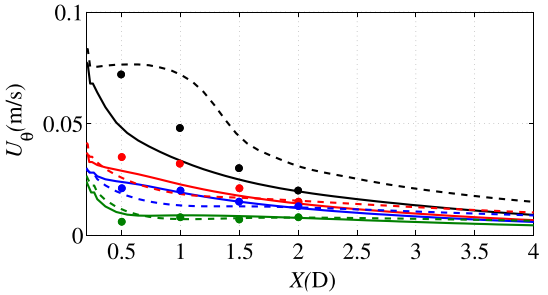

Fig. 16. Variation of tangential velocity U_θ with streamwise position from RANS-BEM with Inlet turbulence (solid curves) and RANS-BEM Tip Turbulence (dashed curves) compared to experiment (●). Comparison shown for radius $r = 0.5R$ (black), $0.75R$ (red), $0.9R$ (blue) and $1.1R$ (green).

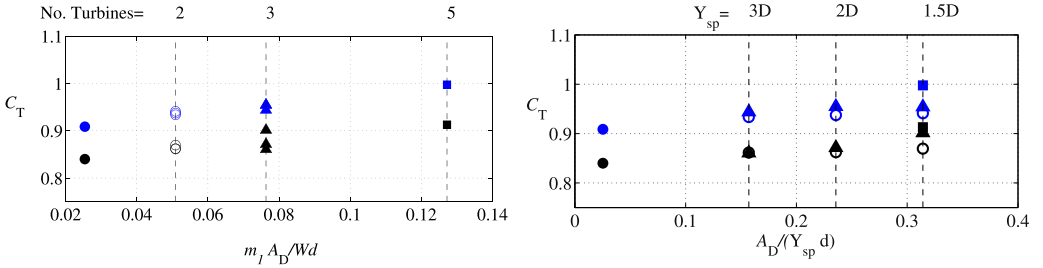

(a) Global Blockage (b) Local Blockage

Fig. 17. Variation of mean thrust coefficient of a single row of rotors with global blockage ($m_1 A_D/Wd$) and local blockage ($A_D/Y_{sp}d$). Data from measurements with single rotor (●) and single rows of two rotors (○), three rotors (▲) and five rotors (■) with transverse spacing Y_{sp} in range $1.5D$ to $3D$. RANS-BEM predictions (blue markers) compared to experiment (black markers).

rows at row spacing of $4D$ and $8D$ that are considered further in Section 6. The mean of the measured tip-speed ratio was imposed for each rotor. Ambient turbulence representing the measured flow was defined based on its suitability for representing the far-wake of a single turbine.

The averaged C_T for a single row of rotors at a number of global and local blockage factors is shown in Fig. 17. Thrust increases relative to a single rotor as may be expected, increasing with both global and local blockage due to increase of onset velocity to each rotor. However, RANS-BEM predictions are consistently greater than measurements, by around 10%. The RANS-BEM and self-similar superposition methods are evaluated for the prediction of the transverse profile of streamwise velocity downstream of the single row of five rotors with a centre-to-centre spacing of $1.5D$ (Fig. 18). The experiments show that close to the rotor the individual wakes are distinct, whilst at distances greater than 8 diameters downstream the wakes have merged. At $X = 4D$ the RANS-BEM gives a good prediction of the maximum velocity deficit behind each rotor. However, the deficit between adjacent wakes is overpredicted and the outward shift of the point of maximum deficit of the wakes either side of the centre is not captured. Individual wakes remain identifiable at $8D$ and $10D$ downstream although experiments indicate merging of all wakes by $X = 8D$. At these distances the superposition approach provides reasonable prediction of both the merged wake profile and bypass velocity.

Fig. 19 shows the discrepancy between experiment and wake model for velocities averaged over the locations of rotors located downstream at row spacing of $4D$, $8D$ and $10D$.Five rotors aligned with the first row and a staggered configuration comprising six rotors located on the y-ordinate between first row rotors are considered. The superposition method is not compared at $4D$ spacing as this location is within the transition between axisymmetric and depth averaged wakes. For the

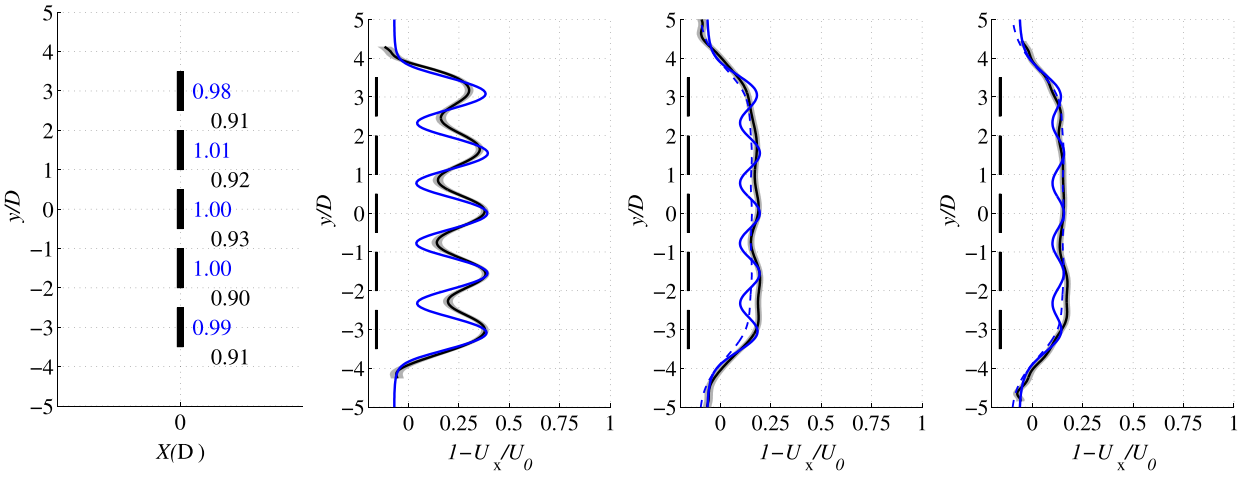

(a) Thrust coefficient. (b) X=4D (c) X=8D (d) X=10D

Fig. 18. Lateral profiles downstream of a single row array of five turbines at lateral centre-to-centre spacing $Y_{sp} = 1.5D$ (array layout 1row5-Y_{sp}1.5D). RANS-BEM (blue text, ——,), Superposition (- - -) and Experiments (black text, ——).

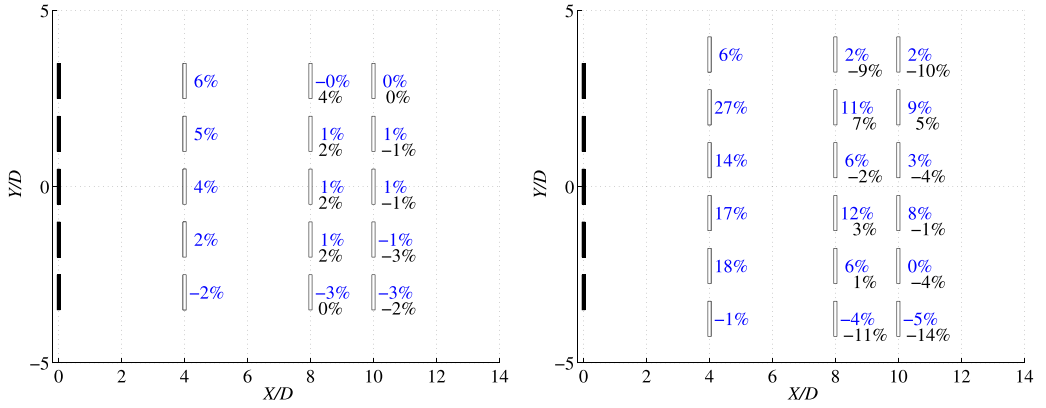

(a) Aligned rotors on downstream rows (b) Staggered rotors on downstream rows

Fig. 19. Percentage discrepancy between RANS-BEM (blue) and superposition of self-similar wakes (black) relative to experiments for the square of the disk average velocity U_D.

Table 4
Summary of discrepancy of U_D^2 using superposition of self-similar wakes and RANS-BEM.

Case	4*D*	8*D*	10*D*
Aligned Rotors			
Superposition	n/a	0% to 4%	3% to 1%
RANS-BEM	−2% to 6%	−3% to 1%	−3 to 1%
Staggered Rotors			
Superposition	n/a	−11% to 7	−14% to 5
RANS-BEM	−1% to 27%	−4% to 12%	−5% to 9

aligned case, velocity at rotors further than 8*D* downstream is predicted to within 3% and 4% root mean square error (RMSE) relative to the experiments for the RANS-BEM and self-similar methods respectively. The range of errors for each method is summarised in Table 4. Lower agreement is observed for the staggered array arrangement where there is overprediction of velocity between individual wakes of upstream rotors.

6. Multi-row array: loading and wake

The loading of turbines on downstream rows has also been considered by direct comparison of RANS-BEM predictions with experimental measurement. This section presents simulations for each of the array layouts detailed in Table 2. For each simulation the mean of the measured tip-speed ratio was imposed for each turbine. Thrust coefficient is defined as measured force normalised to the undisturbed hub height velocity, U_0, and the onset velocity is defined as the rotor averaged velocity defined by the wakes of the upstream rows. Comparison is on the basis of mean thrust although it should be recalled that variation of measured thrust coefficient was observed (see e.g. Figs. 4 and 5). Predicted and measured thrust as a function of imposed tip-speed ratio are presented in Fig. 20 indicating general agreement of variation between rows but typically overprediction of thrust magnitude and different variation of thrust with rotor position relative to the experimental data.

Variation of both mean thrust coefficient and onset velocity with rotor position is shown in Fig. 21 for four multi-row configurations along with transverse profiles of velocity downstream of the array. A summary of the range of thrust coefficient with rotor position and the range of discrepancies between measured and predicted mean thrust is provided in Table 5 for all arrays studied.

For all multi-row cases the rotors on the first row of the array have higher thrust coefficient than a single isolated rotor and rotational speed increases since applied torque is defined as constant. For the two rows of five rotors (Fig. 20(a)), measured thrust on the front row is higher than for a single row of five and there is greater variation along the row with maximum thrust coefficient on the outermost rotors. This along-row variation is not predicted by the RANS-BEM and the individual rotor C_T is within -6 to $+8$%. There is asymmetry of the measured C_T along the second row and this may be associated with the higher velocity bypass flow on one side of the flume (Fig. 21(a,I)). In contrast the RANS-BEM predictions of thrust are symmetric along the row, underpredicting the outermost rotor thrust coefficient by 17% but within 2% for the three inner rotors on the second row.

For both arrays with a front row of three rotors and a second row of four staggered rotors (Fig. 20(b and c)), the measured thrust on the front row is higher than for a single row of three with a reduction of between 12% and 25% varying with rotor location on the second row. Thrust coefficients are generally overpredicted, by up 10% on the front row and 20% on the

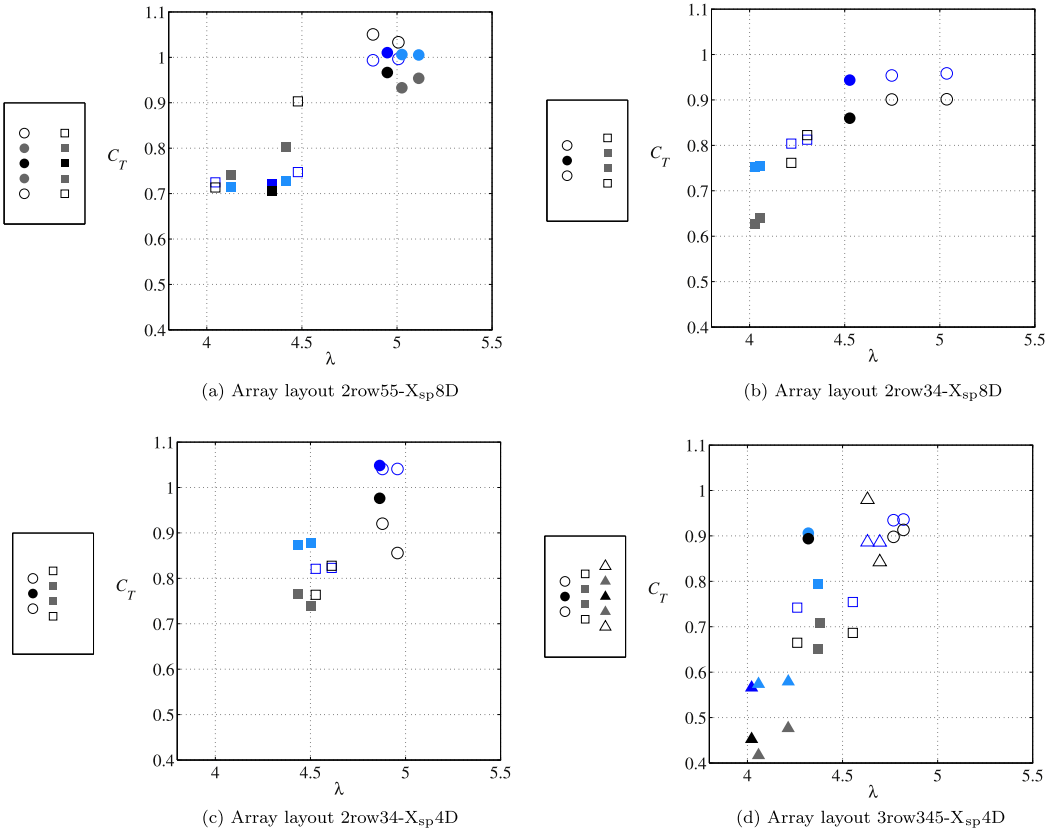

(a) Array layout 2row55-X_{sp}8D (b) Array layout 2row34-X_{sp}8D

(c) Array layout 2row34-X_{sp}4D (d) Array layout 3row345-X_{sp}4D

Fig. 20. Mean thrust (C_T) and tip-speed ratio (λ) for multiple row arrays. Experiments (black), RANS-BEM (Blue).

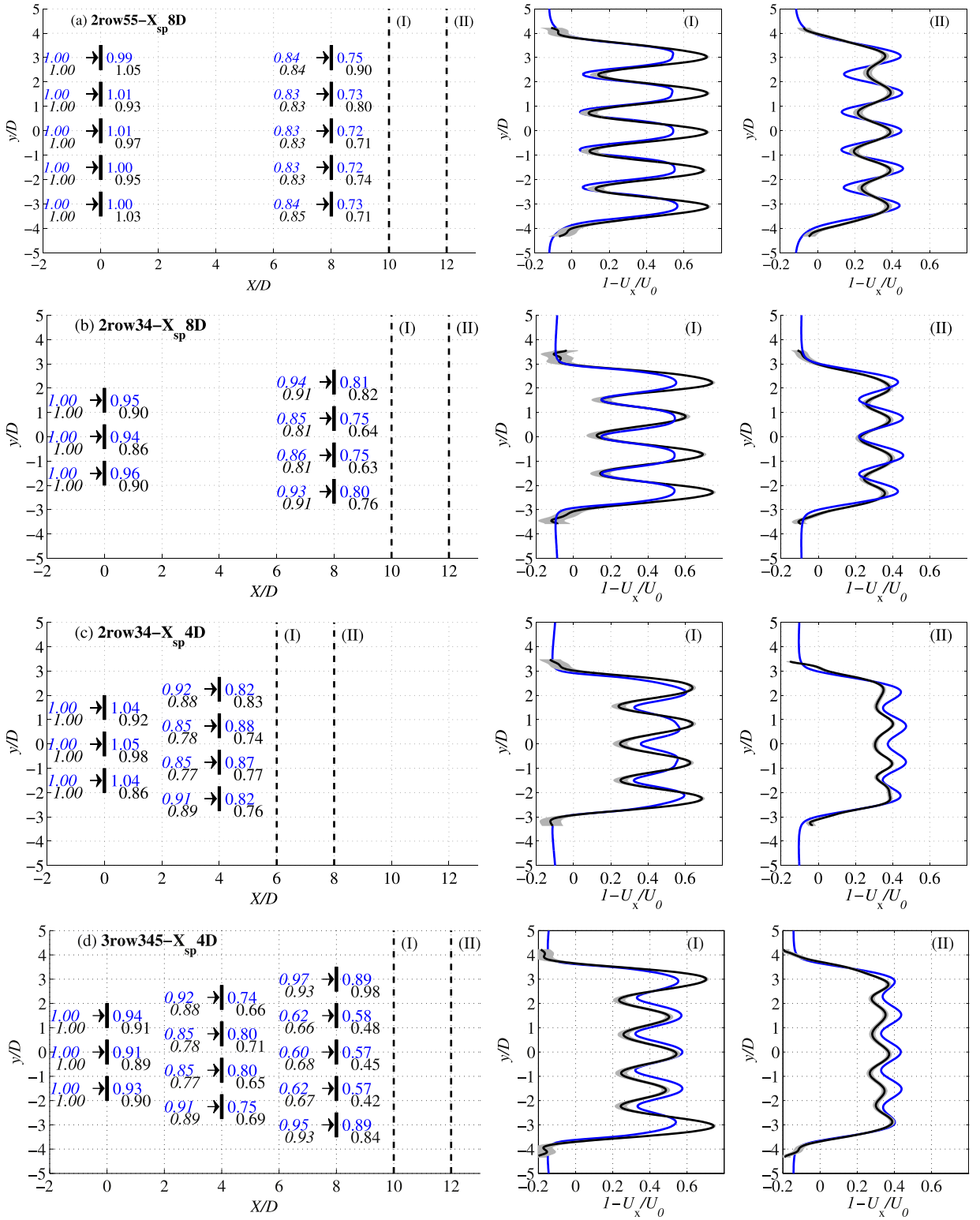

Fig. 21. Mean values of onset velocity (text adjacent to arrow) and thrust coefficient (text downstream of each rotor) from RANS-BEM (blue text) and from experiment (black text). Transverse profile of velocity also shown at (I) $X_{sp}+2D$ and (II) $X_{sp}+4D$ from RANS-BEM (blue curves) and experiment (black curve with grey shading denoting standard deviation).

Table 5
Summary of variation of measured thrust coefficient and RANS blade element prediction accuracy for individual rotors within arrays of up to twelve rotors.

	Case	Row configuration and location[a]	Variation of measured thrust		Accuracy of RANS-BEM	
			Thrust on individual rotors[b]	Aggregate thrust on array[b]	Thrust on individual rotors	Aggregate thrust on array
	Single		+8%	–	–	+8%
1 Row	**1row2-Y_{sp}**1.5D	Front row (direct)	+3 to +4%	4%	+8 to +9%	+8%
	1row2-Y_{sp}3D	Front row (direct)	+1 to +4%	3%	+8 to +10%	+9%
	1row2-Y_{sp}3D	Front row (direct)	+2 to +3%	3%	+8 to +8%	+8%
	1row3-Y_{sp}1.5D	Front row (direct)	+5 to +10%	+7%	+3 to +8%	+6%
		4 Stag. at 4D (U_D^2)a	−40 to −20%		+3 to +21%	
		4 Stag. at 8D (U_D^2)b	−16 to −34%		+5 to +12%	
	1row3-Y_{sp}2D		+3 to +5%	+4%	+9 to +10%	+10%
	1row3-Y_{sp} 3D		+1 to 4%	+2%	+9 to +12%	+10%
	1row5-Y_{sp}1.5D	Front row (direct)	+7 to +10%	+9%	+8 to +11%	+9%
		5 Alig. at 4D (U_D^2)	−48 to −44%		−4 to +5%	
		5 Alig. at 10D (U_D^2)	−32 to −27%		−1 to +2%	
		5 Alig. at 10D (U_D^2)	−28 to −24%		+2 to +5%	
		6 Stag. at 4D (U_D^2)	−42 to −18%		−2 to +28%	
		6 Stag. at 8D (U_D^2)	−34 to −9%		−4 to +12%	
		6 Stag. at 10D (U_D^2)	−31 to −5%		−9 to +10%	
2 Rows	**2row55-X_{sp}8D**	Front row (direct)	+11 to +25%	+5%	−5 to +8%	−2%
		5 aligned at 8D (direct)c	−16 to +7%		−17 to +2%	
	2row34-X_{sp}4D	Front row (direct)	+2 to +16%	−1%	+7 to +22%	+12%
		4 staggered at 4D (direct)a	−12 to −2%		−1 to +19%	
		5 Stag. at 6D(U_D^2)	−58 to −7%		−31 to +19%	
		5 Stag. at 8D(U_D^2)d	−56 to −13%		−23 to +9%	
	2row34-X_{sp}8D	Front row (direct)	+2 to +7%	−6%	+6 to +10%	+8%
		4 staggered at 8D (direct)b	−25 to −2%		−1 to 20%	
3 Rows	**3row345-X_{sp}4D**	Front row (direct)	+6 to +8%	−15%	+1 to +4%	+9%
		4 staggered at 4D (direct)	−23 to −16%		+10 to +22%	
		5 staggered at 8D (direct) d	−50 to +16%		−10 to +38%	

[a] Rows marked "direct" show measured thrust whereas rows marked "U_D^2" show the square of disc averaged velocity over the rotor swept area. Labels a, b, c, d indicate locations for which both disc averaged velocity and directly measured thrust are available from different array configurations.
[b] Relative to single isolated rotor $C_T = 0.84$.

second row. For row spacing of $X_{sp} = 8D$ loading is nearly symmetric and maximum thrust is observed on the outermost rotors of the second row. The relative variation is predicted in this case. Asymmetry is observed for the same configuration with $X_{sp} = 4D$ and this is also evident in the downstream wake measurement although not predicted.

For each case a significant reduction of thrust is observed on all rotors on downstream rows, as compared to an isolated rotor. An exception to this is the final row of the three-row array (3row345-X_{sp}4D, Fig. 20(d)) for which C_T on the outermost rotors of the third row is of similar magnitude to the front row rotors. At these locations the swept area is exposed to the bypass flow that develops past the two upstream rows Fig. 21(b) and so the averaged velocity onset to these rotors is similar to the undisturbed flow, $U_D = 0.99U_0$ (this is from the velocity profile of Fig. 21(c,II)). However, in the centre of this row, thrust coefficient is reduced by up to 50% due to the merged wakes of the two upstream rows. For each configuration thrust variation is slightly asymmetric and this is more pronounced as the aggregated thrust of the array and the bypass velocity increase.

In general the wake prediction for each of the two and three row arrays, shown at 2*D* and 4*D* downstream of the final row is in reasonable agreement with measurement. For the aligned case (2row55-X_{sp}8D) the findings are similar to those for the single row of Section 5 with slightly less mixing between wakes at 4*D* but similar mean deficit. For each of the staggered cases the agreement for the central wakes is similar for all cases. The outermost wakes are similar to the experiments for the two row cases but there is underprediction of maximum deficit for the row spacing of 8*D* (2row34-X_{sp}8D, Fig. 21(b, I)) and overprediction of mean deficit for the row spacing of 4D (2row34-X_{sp}8D, Fig. 21(b, II)). This is similar for the three row case (3row345-X_{sp}4D, Fig. 21(d)).

The discrepancy of thrust for each RANS-BEM disk as compared to experimental measurements is given for each rotor in the Appendix and summarised for each row in Table 5. For each rotor on the front row, except the two outermost rotors on the 2row55-X_{sp}8D layout, the predicted C_T is larger than measured experimentally. This is typically within 10% and 20% for first and second row rotors but greater for rotors on the centre of the third row. Aggregated thrust force of an array is

important for representing the effect of a farm of tidal stream turbines on the ambient flow. This varies from 0.84 to 1.06 times the thrust on the same number of turbines in isolation and is predicted to within 12%. The discrepancies for each of the array cases can be attributed to a combination of factors, the C_T prediction from a single isolated rotor being greater than the experiments, the RANS-BEM producing a narrow wake and thus underpredicting the inter-disk bypass flow, the simulation not including a sheared inflow profile, slight lateral variation of the onset flow, which may amplify bias of the bypass flows, and uncertainties of the experimental measurements.

7. Conclusion

The accuracy of a RANS blade element method for wake and mean thrust prediction has been assessed by comparison to experimental measurement for a single turbine and small arrays of turbines. Experiments were conducted with 3-bladed rotors in a shallow turbulent flow and mean and standard deviation of thrust coefficient were obtained from 136 to 419 samples for each of eleven array configurations. For a single rotor variation of thrust coefficient with tip-speed ratio is generally consistent with measurement for the global blockage of the experiments but overpredicted by 6–8% accounting for the channel geometry and turbulence. With onset turbulence representative of experiments the profile of wake velocity was predicted to a within 8% RMSE from four diameters downstream of a single turbine. Streamwise velocity was predicted to reasonable accuracy within the near-wake for which tangential velocity was also similar to experiment from 1.0*D* downstream and for radii greater than half the radius. Over the near-wake region agreement was slightly improved by incorporation of a tip turbulence source at the rotor circumference based on turbulent kinetic energy distribution predicted by a blade resolved model.

For a single row of rotors increase of thrust due to local and global blockage is in agreement with experiments although the thrust magnitude is overpredicted, by 3–12%, varying with number of turbines and turbine position within the array. The transverse velocity profile downstream of a single row of five turbines at centre to centre spacing of 1.5*D* is similar to measured although the initial deficit is underpredicted and there is less mixing between adjacent wakes throughout the array wake. The square of the velocity averaged over the disc area (U_D^2) provided a metric to quantify the accuracy of loading of downstream turbines. This was within 5% of measurements at a second row of rotors aligned with the front row located 4*D* downstream and beyond, and within 12% at a second row of rotors in a staggered arrangement. Similar agreement was obtained based on superposition of the self-similar wake of individual turbines with an onset flow adjusted to maintain mass continuity.

For arrays of two and three rows at 4D and 8D spacing, the accuracy of load prediction varies with position within the array with discrepancy typically less than 10% for the front row, 20% for the second row and up to 38% for the third row considered. Increased thrust on the front row relative to a single row is typically predicted. Largest discrepancies occur for the inner rotors on downstream rows wholly in the wakes of upstream rotors. Asymmetry is evident for higher numbers of turbines, associated with bias of the bypass flow around one side of the array. For row spacings of 8D or more individual thrust error is less than 18% giving velocity errors less than 9% but power error of up to 28%. The accuracy of RANS-BEM using commercially available software thus has been assessed for the complex wake flows of arrays of up to twelve 3-bladed rotors.

Acknowledgements

This work was supported by an EPSRC Supergen Marine PhD studentship and the EPSRC Grant EP/M020304/1 (ALLTTIDAL). Experiments were also conducted as part of the EPSRC grant EP/J010235/1 (X-MED). Data associated with this study is available at DOI: 10.13140/RG.2.1.3842.6482. The experimental equipment and part of the experimental database was developed during the Performance of Arrays of Wave and Tidal Array Systems (PerAWaT) project commissioned by the Energy Technologies Institute (ETI). Discussions with members of the PerAWaT consortium and particularly Jo Chetwood (nee Whelan), Mat Thomson, and Steve Parkinson are appreciated.

Appendix

See Fig. 22.

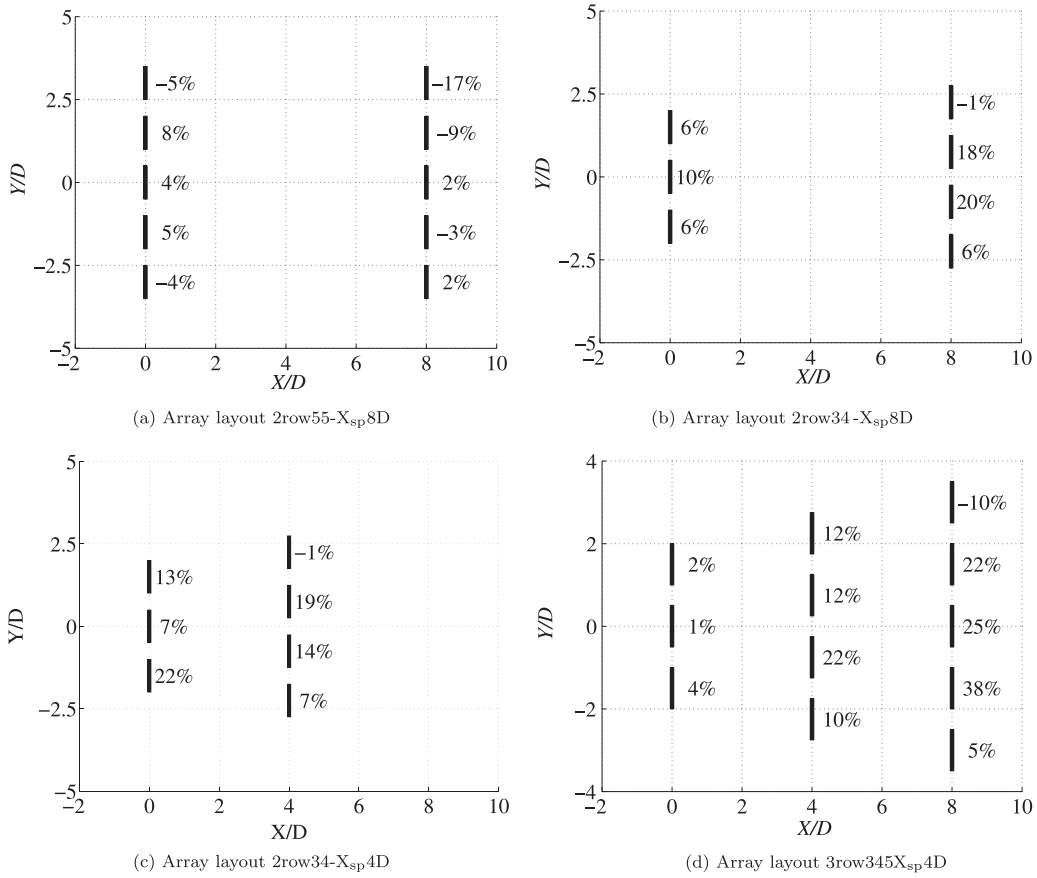

(a) Array layout 2row55-X_{sp}8D

(b) Array layout 2row34-X_{sp}8D

(c) Array layout 2row34-X_{sp}4D

(d) Array layout 3row345X_{sp}4D

Fig. 22. Percentage difference of thrust coefficient C_T between RANS-BEM predictions and experimental measurements for the four different multi-row array layouts considered.

References

Afgan, I., McNaughton, J., Rolfo, S., Apsley, D.D., Stallard, T., Stansby, P., 2013. Turbulent flow and loading on a tidal stream turbine by LES and RANS. Int. J. Heat Fluid Flow 43 (October), 96–108.

Ainslie, J.F., 1988. Calculating the flowfield in the wake of wind turbines. J. Wind Eng. Ind. Aerodyn. 27 (1–3), 213–224.

Bahaj, A.S., Batten, W.M.J., McCann, G., 2007. Experimental verifications of numerical predictions for the hydrodynamic performance of horizontal axis marine current turbines. Renew. Energy 32 (December (15)), 2479–2490.

Batten, W.M.J., Bahaj, A.S., Myers, L., 2013. Accuracy of the actuator disc-RANS approach for predicting the performance and wake of tidal turbines. Philos. Trans. R. Soc. A: Math. Phys. Eng. Sci. A 371, 20120293.

Chamorro, L.P., Arndt, R.E.A., Sotiropoulos, F., 2012. Reynolds number dependence of turbulence statistics in the wake of wind turbines. Wind Energy 15, 733–742.

Churchfield, M., Li, Y., Moriarty, P.J., 2013. A large-eddy simulation study of wake propagation and power production in an array of tidal-current turbines. Philos. Trans. R. Soc. A: Math. Phys. Eng. Sci. A 371 (December), 20120421.

Edmunds, M., Malki, R., Williams, A., Masters, I., Croft, T.N., 2014. Aspects of tidal stream turbine modelling in the natural environment using a coupled BEM-CFD model. Int. J. Mar. Energy 7 (September), 20–42.

Fleming, C., McIntosh, S., Willden, R.H.J., August 2013. Tidal turbine performance in sheared flow. In: 10th European Wave and Tidal Energy Conference. Aalborg, Denmark.

Hansen, M., 2008. Aerodynamics of Wind Turbines, 2nd ed. Earthscan, London.

Harrison, M.E., Batten, W.M.J., Myers, L., Bahaj, A.S., 2010. Comparison between CFD simulations and experiments for predicting the far wake of horizontal axis tidal turbines. IET Renew. Power Gener. 4 (September (6)), 613–642.

Lloyd, T.P., Turnock, S.R., Humphrey, V.F., 2014. Assessing the influence of inflow turbulence on noise and performance of a tidal turbine using large eddy simulations. Renew. Energy 71 (November), 742–754.

Malki, R., Masters, I., Williams, A.J., Croft, T.N., 2014. Planning tidal stream turbine array layouts using a coupled blade element momentum – computational

fluid dynamics model. Renew. Energy 63 (March), 46–54.
Maskell, E., 1965. A Theory of the Blockage Effects on Bluff Bodies and Stalled Wings in a Closed Wind Tunnel. Technical Report 3400, Aeronautical Research Council Reports and Memoranda.
Masters, I., Malki, R., Williams, A.J., Croft, T.N., 2013. The influence of flow acceleration on tidal stream turbine wake dynamics: a numerical study using a coupled BEM-CFD model. Appl. Math. Model. 37 (September (16–17)), 7905–7918.
Masters, I., Williams, A., Croft, T., Togneri, M., Edmunds, M., Zangiabadi, E., Fairley, I., Karunarathna, H., 2015. A comparison of numerical modelling techniques for tidal stream turbine analysis. Energies 8 (August (8)), 7833–7853.
McNaughton, J., Rolfo, S., Apsley, D., Afgan, I., Stansby, P.K., Stallard, T.J., November 2012. CFD prediction of turbulent flow on an experimental tidal stream turbine using RANS modeling. In: 1st Asian Wave and Tidal Energy Conference. Jeju Island, Korea.
Miley, S., 1982. A Catalog of Low Reynolds Number Airfoil Data for Wind Turbine Applications. Technical Report DE82-021712, NTIS.
Nishino, T., Wilden, R.H.J., 2012. Low-order modelling of blade-induced turbulence for RANS actuator disk computations of wind and tidal turbines. In: EUROMECH Colloquium Wind Energy and the Impact of Turbulence on the Conversion Process. Oldenburg, Germany.
Nishino, T., Willden, R.H.J., 2012. Effects of 3-D channel blockage and turbulent wake mixing on the limit of power extraction by tidal turbines. Int. J. Heat Fluid Flow 37 (October (C)), 123–135.
Parkinson, S.G., Stallard, T., Thomson, M., Wickham, A., Willden, R., October 2012. Comparison of scale model wake data with an energy yield analysis tool for tidal turbine farms. In: 4th International Conference on Ocean Energy. Dublin, Ireland.
Pope, S.B., August 2000. Turbulent Flows. Cambridge University Press, New York.
Schluntz, J., Willden, R.H.J., 2014. An actuator line method with novel blade flow field coupling based on potential flow equivalence. Wind Energy 18 (June (8)), 1469–1485.
Shives, M., Crawford, C., 2014. Turbulence modelling for accurate wake prediction in tidal turbine arrays. In: 5th International Conference on Ocean Energy, 4–6 November, Halifax, Nova Scotia.
Sørensen, J.N., Shen, W.Z., 2002. Numerical modeling of wind turbine wakes. J. Fluids Eng. 124 (2), 393.
Stallard, T., Collings, R., Feng, T., Whelan, J., 2013. Interactions between tidal turbine wakes: experimental study of a group of three-bladed rotors. Philos. Trans. R. Soc. A: Math. Phys. Eng. Sci. 371 (January (1985)), 20120159.
Stallard, T., Feng, T., Stansby, P.K., 2015. Experimental study of the mean wake of a tidal stream rotor in a shallow turbulent flow. J. Fluids Struct. 54 (April), 235–246.
Stansby, P., Stallard, T., 2016. Fast optimisation of tidal stream turbine positions for power generation in small arrays with low blockage based on superposition of self-similar far-wake velocity deficit profiles. Renew. Energy 92, 366–375.
Sutherland, D., Seller, B., Harding, S., Bryden, I., July 2013. Initial flow characterisation utilising turbine and seabed installed acoustic sensor arrays. In: 10th European Wave and Tidal Energy Conference. Aalborg, Denmark.
Tedds, S.C., Poole, R.J., Owen, I., 2012. Wake characteristics of horizontal axis tidal stream turbines in uniform and non-uniform steady flows. In: 4th International Conference on Ocean Energy. Dublin, Ireland.
Thomson, J., Polagye, B., Durgesh, V., Richmond, M.C., 2012. Measurements of turbulence at two tidal energy sites in puget sound, WA. IEEE J. Ocean. Eng. 37 (July (3)), 363–374.
Thomson, M., Stallard, T., Collings, R., May 2011. Array Scale Experiments Test Report. Technical Report WG4 WP2 D5, ETI Marine Programme Project PerAWAT MA1003, Garrad Hassan & Partners Ltd. Doc. No. 104331/BR/02.
Togneri, M., Masters, I., James, O., 2011. Incorporating turbulent inflow conditions in a blade element momentum model of tidal stream turbines. In: 1st International Offshore and Polar Engineering Conference. Maui, Hawaii, USA.
Turnock, S.R., Phillips, A.B., Banks, J., Nicholls-Lee, R., 2011. Modelling tidal current turbine wakes using a coupled RANS-BEMT approach as a tool for analysing power capture of arrays of turbines. Ocean Eng. 38, 1300–1307.
Way, S., Collier, W., July 2013. Full-scale validation study of a numerical tool for the prediction of the loading and hydrodynamic performance of axial flow tidal turbines. In: 10th European Wave and Tidal Energy Conference. Aalborg, Denmark.
Whelan, J.I., Stallard, T., 2011. Arguments for modifying the geometry of a scale model rotor. In: 9th European Wave and Tidal Energy Conference (EWTEC). Southampton, UK.